Suppression of Fe-cation migration by indium substitution in LiFe2-xInxSbO6 cathode materials

MARTÍNEZ DE IRUJO LABALDE, Xabier, GRIEVSON, Heather, MORTIMER, Josie-May, BOOTH, Samuel, SCRIMSHIRE, Alex, BINGHAM, Paul <http://orcid.org/0000-0001-6017-0798>, SUARD, Emmanuelle, CUSSEN, Serena and HAYWARD, Michael

CHEMISTRY OF MATERIALS

pubs.acs.org/cm

Article

Suppression of Fe-Cation Migration by Indium Substitution in $LiFe_{2-x}In_xSbO_6$ Cathode Materials

Xabier Martínez de Irujo Labalde, Heather Grievson, Josie-May Mortimer, Samuel G. Booth, Alex Scrimshire, Paul A. Bingham, Emmanuelle Suard, Serena A. Cussen, and Michael A. Hayward*

Cite This: https://doi.org/10.1021/acs.chemmater.2c03418

Read Online

ACCESS | Metrics & More | Article Recommendations | Supporting Information

ABSTRACT: Cation migration on electrochemical cycling can significantly influence the performance of li-ion cathode materials. Phases of composition $LiFe_{2-x}In_xSbO_6$ ($0 < x < 1$) adopt crystal structures described in space group *Pnnm*, consisting of a hexagonally close-packed array of oxide ions, with Fe/In and Sb cations ordered on octahedral sites, and lithium cations located within partially occupied tetrahedral sites. NPD, SXRD, and ^{57}Fe Mössbauer data indicate that on reductive lithium insertion (either chemically or electrochemically), $LiFe_2SbO_6$ is converted to $Li_2Fe_2SbO_6$ accompanied by large-scale cation migration, to form a partially Fe/Li cation-ordered and Fe^{2+}/Fe^{3+} charge-ordered phase from which lithium cations cannot be easily removed, either chemically or electrochemically. Partial substitution of Fe with In suppresses the degree of cation migration that occurs on lithium insertion such that no structural change is observed when $LiFeInSbO_6$ is converted into $Li_{1.5}FeInSbO_6$, allowing the system to be repeatedly electrochemically cycled between these two compositions. Phases with intermediate levels of In substitution exhibit low levels of Fe migration on Li insertion and electrochemical capacities which evolve on cycling. The mechanism by which the In^{3+} cations suppress the migration of Fe cations is discussed along with the cycling behavior of the $LiFe_{1.5}In_{0.5}SbO_6$–$Li_{1.75}Fe_{1.5}In_{0.5}SbO_6$.

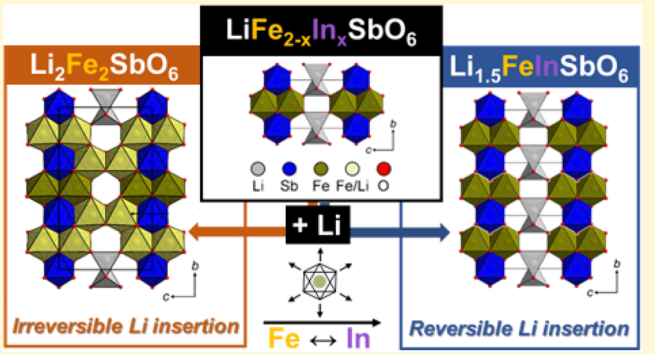

INTRODUCTION

Rechargeable Li-ion batteries have transformed daily life by providing a compact power source applicable to a broad spectrum of technologies ranging from personal items such as portable telephones to larger-scale devices such as electric vehicles. However, the majority of cathode materials currently employed in Li-ion systems are based on rare, expensive, and toxic elements, such as cobalt or nickel.[1−3] If Li-ion systems are to be widely used, particularly in energy storage for renewable power generation or in vehicles, more sustainable materials based on more earth abundant elements need to be developed.[4,5]

In this context, the high abundance, low cost, and low toxicity of iron compounds make iron-based cathode materials attractive.[6] However, there are a number of obstacles that hamper the development of high capacity, high energy density Fe-based cathode materials. For example, utilizing the $Fe^{III/IV}$ redox couple in Li−Fe−M−O systems is challenging, with irreversible anion redox process and/or oxygen loss widely observed.[7,8] In addition, iron-oxide-based cathode materials tend to exhibit extensive cation migration during charge and discharge cycles.[9] This arises because Fe^{3+} cations adopt high-spin, $S = {}^5/_2$ configurations in oxide environments, and thus have no strong ligand-field-based coordination geometry preference, with both tetrahedral and octahedral coordinations common. In contrast, $S = 2$ Fe^{2+} and Fe^{4+} cations favor octahedral coordination which, when combined with the large change in ionic radius of Fe cations as a function of oxidation state (Fe^{2+}: 0.78 Å, Fe^{3+}: 0.645 Å, Fe^{4+}: 0.585Å),[10] provides a large driving force for undesirable structural rearrangements during the cycling of Fe-based cathode materials. These two effects can be seen during the cycling of the different polymorphs of $LiFeO_2$, which are irreversibly converted to $LiFe_5O_8$ on lithium extraction,[8,11,12] with accompanying Fe-cation migration and oxygen loss.

Some of the issues associated with the $Fe^{III/IV}$ redox couple can be avoided by changing to the $Fe^{II/III}$ redox couple, with the associated loss in output potential mitigated by switching the anions in the system from simple O^{2-} oxide ions to large polyatomic anions such as PO_4^{3-}.[13] However, while materials of this type, such as $LiFePO_4$, can achieve good gravimetric

Received: November 14, 2022
Revised: December 14, 2022

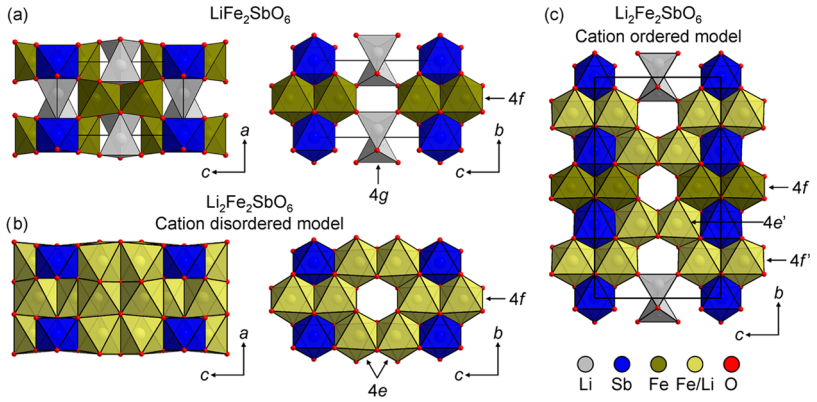

Figure 1. Crystal structure of (a) $LiFe_2SbO_6$ and (b) the cation-disordered and (c) cation-ordered structures of $Li_2Fe_2SbO_6$.

capacities (~170 mAh g^{-1}) the relatively low crystallographic density of these materials can result in relatively poor volumetric capacities.[6]

Recently, we have demonstrated that it is possible to stabilize high oxidation states of iron, in materials such as $LiFeSbO_5$, without oxygen loss.[14] However, large-scale cation migration on lithium extraction prevents electrochemical cycling of this material. Here, we describe how cation substitution can be used to suppress large-scale cation migration in the $Fe^{II/III}$ cathode material $LiFe_{2-x}In_xSbO_6$ to facilitate repeated electrochemical cycling.

EXPERIMENTAL SECTION

Synthesis. Polycrystalline samples of $LiFe_{2-x}In_xSbO_6$ (x = 0, 0.25, 0.5, 0.75 and 1) were synthesized by a ceramic method. Suitable ratios of Fe_2O_3 (Alfa Aesar, 99.995%), Sb_2O_3 (Alfa Aesar, 99.999%) In_2O_3 (Alfa Aesar, 99.995%), and a 5% excess of Li_2CO_3 (Alfa Aesar, 99.95%) were ground together using an agate pestle and mortar. The mixtures were then placed in alumina crucibles and heated in air at 600 °C for 12 h. The powders were then reground, pressed into 13 mm pellets, and heated in air at 1050 °C for three cycles of 12 h with intermediate grindings.

Attempts to intercalate additional lithium within samples were performed by stirring approximately 2 g of material in 15 mL of a 1.4 M solution of *n*-BuLi in toluene (Sigma-Aldrich), under a nitrogen atmosphere, for 5 days at room temperature. Samples were then filtered and washed with clean toluene under a nitrogen atmosphere on a Schlenk line. After lithiation, the samples were stored under inert atmosphere in an argon-filled glovebox.

Chemical oxidation reactions were carried out by stirring the lithiated material with I_2 in acetonitrile for 4 h at room temperature. Samples were then filtered and washed with clean acetonitrile and then acetone, in air.

Characterization. Reaction progress and initial structural characterization was performed using laboratory powder X-ray diffraction (PXRD) data collected using a PANalytical X'Pert diffractometer incorporating an X'celerator position-sensitive detector (monochromatic Cu Kα1 radiation). High-resolution synchrotron X-ray powder diffraction (SXRD) data were collected using the I11 instrument at the Diamond Light Source Ltd. Diffraction patterns were collected using Si-calibrated X-rays with an approximate wavelength of 0.825 Å from samples, sealed in 0.3 mm diameter borosilicate glass capillaries. Neutron powder diffraction (NPD) data were collected using the D2B diffractometer (λ = 1.594 Å) at the ILL neutron source, from samples sealed under argon in 8 mm vanadium cans. Rietveld refinement was performed using the TOPAS suite of programs (v6).[15]

^{57}Fe Mössbauer spectroscopy measurements utilized acrylic absorber disks with a sample area of 1.767 cm^2, which were loaded to present 2.16 × 10^{-3} g cm^{-2} of Fe, and achieve a Mössbauer thickness of 1. Samples were homogeneously mixed with graphite powder to achieve this level of loading. The 14.4 keV γ-rays were supplied by the cascade decay of 25 mCi ^{57}Co in a Rh matrix source, oscillated at constant acceleration by a SeeCo W304 drive unit, and detected using a SeeCo 45431 Kr proportional counter operating with a 1.745 kV bias voltage applied to the cathode. All measurements were calibrated relative to α-Fe foil. Spectral data were fitted using the Recoil software package,[16] using Lorentzian line shapes, to determine the center shift (CS), quadrupole splitting (Δ) hyperfine magnetic field (B_{hf}), half-width at half-maximum (HWHM) linewidth, and spectral area of each contributing signal.

X-ray absorption experiments were performed at the B18 beamline of the Diamond Light Source. The measurements were carried out using the Pt-coated branch of the collimating and focusing mirrors, a Si(111) double-crystal monochromator, and a pair of harmonic rejection mirrors. The size of the beam at the sample position was approximately 600 μm × 700 μm. X-ray absorption near-edge spectroscopy (XANES) data were collected at the Fe-K edge (7112 eV) in transmission mode with ion chambers before and behind the sample filled with appropriate mixtures of inert gases to optimize sensitivity (I_0: 300 mbar of N_2 and 700 mbar of He, resulting in an overall efficiency of 10%; I_t: 150 mbar of Ar and 850 mbar of He, with 70% efficiency). The spectra were measured with a step size equivalent to 0.25 eV. Data were normalized using the program Athena[17] with a linear pre-edge and polynomial post-edge background subtracted from the raw $\ln(I_t/I_0)$ data. The samples were prepared in the form of a self-supported pellet, with the thickness optimized to obtain an edge jump close to 1.

Electrochemical Characterization. The electrode material was formed from a mixture of active material, electronically conductive carbon black C-NERGY Super C65 (Imerys Graphite & Carbon, Belgium), and PVDF (poly(vinylidene fluoride)) (MTI Corporation) as a binder, in a ratio of 8:1:1. The materials were ground using an Agate pestle and mortar for 15 min. A slurry was made by adding NMP (*N*-methyl-2-pyrrolidone) (Merck, Germany) and mixed using a Thinky ARE-250 mixer (Intertronics, U.K.). The slurry was cast on carbon-coated aluminum foil using an MTI MSK-AFA-L800 tape caster (MTI Corporation) with a blade height of 150 um, providing a cathode loading of 3.8 +/− 1.2 mg cm^{-1}. The cathode film was dried at 80 °C, before being transferred to an 80 °C vacuum oven for a minimum of 16 h. Cathodes were cut to 12 mm using an MTI disk cutter (MTI Corporation). CR2032 SS316 coin cells were assembled using the cathodes, 16 mm separators cut from Whatman glass microfibre (GF/F grade) (Merck, Germany), and pre-cut 15.6 mm lithium chips of 0.25 mm thickness (Cambridge Energy Solutions Ltd., U.K.) were used as the anode. The electrolyte was 1 M $LiPF_6$ in ethylene carbonate and ethyl methyl carbonate 3:7 v/v (Solvionic, France). CV measurements were conducted using a Biologic VMP-300 potentiostat at room temperature, and the galvanostatic cycling measurements were conducted using a MACCOR Series 4000 analyzer (Maccor) at 25 °C.

https://doi.org/10.1021/acs.chemmater.2c03418
Chem. Mater. XXXX, XXX, XXX−XXX

RESULTS

Structural Characterization of $LiFe_{2-x}In_xSbO_6$ ($0 < x < 1$). SXRD and NPD data collected from $LiFe_2SbO_6$ ($x = 0$) at room temperature could be indexed using an orthorhombic unit cell ($a = 4.913$ Å, $b = 5.133$ Å, $c = 8.454$ Å). The observed reflection conditions: $0kl$: $k+l = 2n$, $h0l$: $h+l = 2n$, $h00$: $h = 2n$, $0k0$: $k = 2n$ and $00l$: $l = 2n$ are consistent with two space groups $Pnn2$ (#34) and $Pnnm$ (#58). A series of structural models were constructed in both space groups, with the best fit to the data achieved using a model in space group $Pnnm$ directly analogous to the reported structure of $LiIn_2SbO_6$,[18] shown in Figure 1a. The NPD data gave no indication of Li/Fe anti-site disorder, or ordering of the Li cations within the 4g cation sites, as is observed in the $Pmn2_1$ symmetry structure of $LiSc_2SbO_6$.[19] Close inspection of the NPD data revealed a series of low-angle peaks with additional intensity compared to the pattern predicted for the structural model. ^{57}Fe Mössbauer data (*vide infra*) indicate that $LiFe_2SbO_6$ is magnetically ordered at room temperature, so the additional diffraction intensity was attributed to magnetic scattering. A symmetry analysis[20,21] revealed that the scattering could be accounted for using a magnetic model, described in space group 58.395 in which the Fe moments were aligned parallel to the *y*-axis, and arranged in an antiferromagnetic configuration, as shown in Figure S1, in the Supporting Information. Full details of the structural and magnetic refinement of $LiFe_2SbO_6$ are given in Table S1 in the Supporting Information, with selected bond lengths in Table S3 and a plot of the data shown in Figure 2.

SXRD and NPD data collected from $LiFeInSbO_6$ ($x = 1$) could also be indexed using an orthorhombic unit cell and fit by a structural model based on the $Pnnm$ structure of $LiFe_2SbO_6$, with a 1:1 disordered combination of Fe/In on the 4*f* crystallographic site, which is occupied by Fe alone in $LiFe_2SbO_6$. There is no indication of magnetic order in $LiFeInSbO_6$ in either ^{57}Fe Mössbauer or NPD data. Full details of the structural refinement of $LiFeInSbO_6$ are given in Table S2 in the Supporting Information, with selected bond lengths in Table S3 and a plot of the data shown in Figure 2.

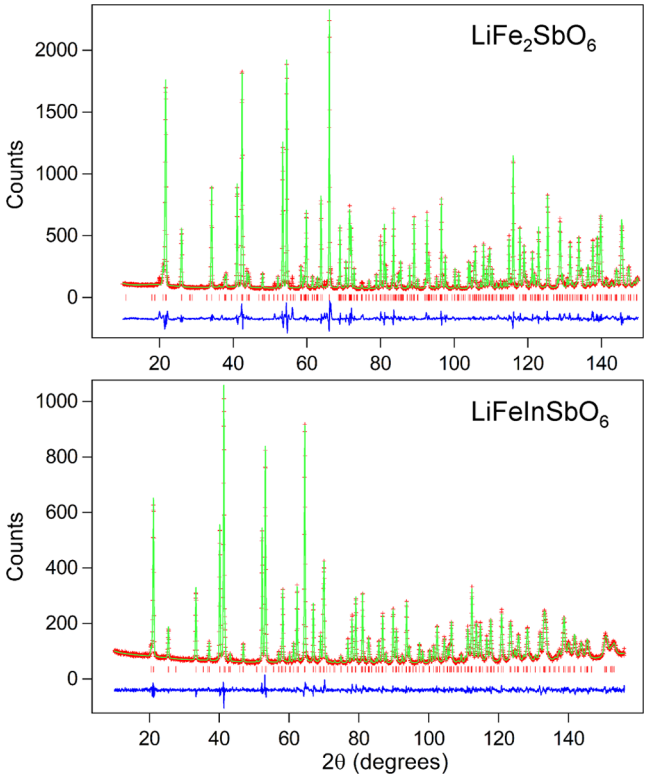

Figure 2. Observed, calculated, and difference plots from the structural and magnetic refinement of $LiFe_2SbO_6$ (top) and $LiFeInSbO_6$ (bottom) against NPD data collected at room temperature.

SXRD data collected from samples of intermediate $LiFe_{2-x}In_xSbO_6$ ($x = 0.25, 0.5, 0.75$) compositions could also be indexed using orthorhombic cells and fit using structural models intermediate between those refined for $LiFe_2SbO_6$ and $LiFeInSbO_6$ with appropriate Fe/In solid solutions on the 4*f* site. Full details of the structural refinements of $LiFe_{2-x}In_xSbO_6$ ($x = 0.25, 0.5, 0.75$) are given in Table S4 in the Supporting Information. The lattice parameters of $LiFe_{2-x}In_xSbO_6$ phases vary smoothly with composition, as shown in Figure 3, in agreement with Vergard's law.

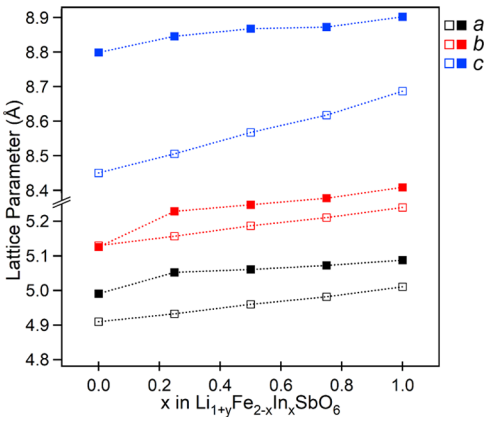

Figure 3. Plot of lattice parameters as a function of composition for $LiFe_{2-x}In_xSbO_6$ (open symbols) and lithiated $Li_{1+y}Fe_{2-x}In_xSbO_6$ (filled symbols).

Structural Characterization of $Li_{1+y}Fe_{2-x}In_xSbO_6$ ($0 < x < 1$). Reaction between $LiFe_{2-x}In_xSbO_6$ ($0 < x < 1$) and *n*-BuLi yields crystalline phases of nominal composition $Li_{1+y}Fe_{2-x}In_xSbO_6$. SXRD data collected from these lithiated phases can be indexed using $Pnnm$-symmetry orthorhombic cells, which are significantly expanded compared to the corresponding $LiFe_{2-x}In_xSbO_6$ parent phases, as indicated by their lattice parameters which are plotted in Figure 3.

Close inspection of the SXRD data collected from lithiated $Li_{1+y}Fe_2SbO_6$ showed strong enhancement of several diffraction peaks ((002), (110), (103)) compared to the unlithiated "parent" material (Figure 4), suggesting a structural change had occurred on lithium insertion. Analogous data collected from other lithiated $Li_{1+y}Fe_{2-x}In_xSbO_6$ phases show a decline in the enhancement of these diffraction reflections with increasing indium content (x) (Figure S7, Supporting Information) so that the $x = 1$ phase, $Li_{1+y}FeInSbO_6$, has diffraction peak intensities which are very similar to the unlithiated parent phase, as shown in Figure 4.

To better characterize the structures of the lithiated phases, NPD data were collected from $Li_{1+y}Fe_2SbO_6$ and $Li_{1+y}FeInSbO_6$. The NPD data collected from $Li_{1+y}FeInSbO_6$ could be fit well by a model based on the refined structure of $LiFeInSbO_6$, with additional lithium cations located on the 4*g* ($x \sim 0.9$, $y \sim 0.8$, 1/2) sites, as shown in Figure 5, to yield a

https://doi.org/10.1021/acs.chemmater.2c03418
Chem. Mater. XXXX, XXX, XXX−XXX

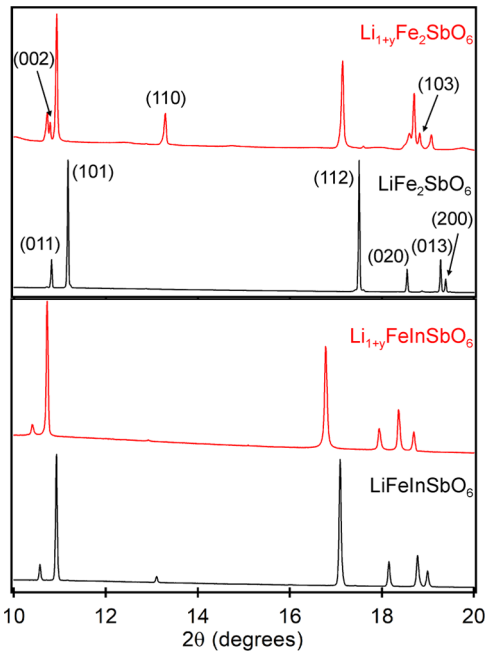

Figure 4. Comparison of SXRD data from $LiFe_2SbO_6$ and lithiated $Li_{1+y}Fe_2SbO_6$ (top) and $LiFeInSbO_6$ and lithiated $Li_{1+y}FeInSbO_6$ (bottom), indexed using units cells $a \sim 4.9$ Å, $b = 5.15$ Å, $c = 8.5$ Å.

composition of $Li_{1.5}FeInSbO_6$ as detailed in Table S5 in the Supporting Information, with selected bond lengths detailed in Table S6.

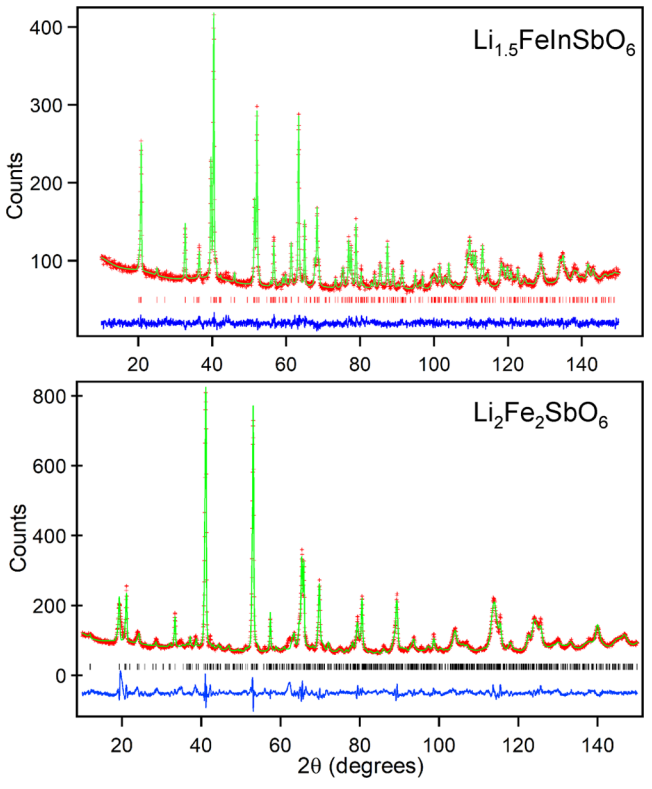

Figure 5. Observed, calculated, and difference plots from the structural refinement of $Li_{1.5}FeInSbO_6$ (top) and $Li_2Fe_2SbO_6$ (bottom) against NPD data collected at room temperature.

In contrast, attempts to fit the NPD data collected from $Li_{1+y}Fe_2SbO_6$ using a model based on the structure of $LiFe_2SbO_6$ were unsuccessful, with multiple intensity mismatches between observed and calculated data and some additional diffraction peaks observed, which were not indexed by the orthorhombic unit cell, as shown in Figure S2 in the Supporting Information.

In an attempt to determine the crystal structure of $Li_{1+x}Fe_2SbO_6$, we first examined the SXRD data collected from this phase and observed that the fit to this data could be significantly improved by transferring $^1/_3$ of the Fe cations located on the 4*f* (1/2, 0, $z \sim 0.3$) octahedral sites to a 4*e* (0, 0, $z \sim 0.64$) octahedral site, with lithium cations distributed between these 4*f* and 4*e* sites, to yield a "cation-disordered" model of composition $Li_2Fe_2SbO_6$, shown in Figure 1b and detailed in Table S7. This cation-disordered model also led to a significant improvement to the fit to the NPD data collected from $Li_{1+x}Fe_2SbO_6$, but as shown in Figure S6, there remained a number of diffraction peaks, which were unindexed by this model. Close inspection of the NPD data revealed that these unindexed peaks could be accounted for by an orthorhombic unit cell with a threefold expansion of the *b*-axis (a = 4.9986(3) Å, b = 15.390(1) Å, c = 8.8040(4) Å) with reflection conditions consistent with space group *Pnnm* (#58). Thus, a "cation-ordered" structural model was constructed in which $^1/_3$ of the Fe cations are located on fully occupied 4*f* sites, $^1/_3$ of the Li cations are located on fully occupied tetrahedral 4*g* sites, with the remaining Fe and Li cations disordered over the remaining octahedral sites, as shown in Figure 1c. It should be noted that the two Fe/Li disordered octahedral sites, labeled 4*e*′ and 4*f*′ in Figure 1c, are actually 8*h* symmetry sites in the expanded cell (as described in Table S8), but we will refer to them using the 4*e*′ and 4*f*′ to make parallels to the small disordered cell. This cation-ordered structural model accounts for the majority of the additional diffraction peaks observed in the NPD data as shown in Figure 5, with a full description of the refined model given in Table S8 and selected bond lengths detailed in Table S9.

It can be seen in Figure S4 that the "super cell" diffraction peaks which require cell tripling are rather broad and asymmetric. This suggests that the ordering of the 4*f* Fe and 4*g* Li sites within the array of cation-disordered 4*f*′ and 4*e*′ sites is not complete. Indeed, there are some diffraction features which are not accounted for by this model but can be fit by a 6-fold expansion of the $LiFe_2SbO_6$ unit cell, suggesting that a number of different cation orderings coexist within the material, with rigorous cation order only observed on relatively short length scales. However, the data show that the cation-ordered structure shown in Figure 1c is the best general description of lithiated $Li_2Fe_2SbO_6$.

The migration of the Fe cations from the 4*f* sites on lithiation is primarily responsible for the change in the intensities of the (002), (110), and (103) diffraction peaks in the SXRD data collected from $Li_{1+y}Fe_2SbO_6$. This data set could be fitted well by the cation-ordered model, as shown in Figure S8 in the Supporting Information. However, indium-containing $Li_{1+y}Fe_{2-x}In_xSbO_6$ phases ($x > 0$) show no indication of strong cation order, so SXRD data from these phases were fit using the cation-disordered model shown in Figure 1b, which achieved good fits to these data sets (Figure S8) and reveals that the fraction of Fe cations which migrate to the 4*e* coordination sites declines with increasing indium substitution (x) as detailed in Table S10 in the Supporting

https://doi.org/10.1021/acs.chemmater.2c03418
Chem. Mater. XXXX, XXX, XXX−XXX

Information. From the SXRD data, it is not possible to unambiguously determine the location of the lithium cations in the $Li_{1+y}Fe_{2-x}In_xSbO_6$ ($0.25 < x < 0.75$) phases, so we have assumed they are distributed over the 4*f* and 4*e* sites occupied by the Fe cations, as observed for $Li_2Fe_2SbO_6$.

XANES Data. Normalized XANES data collected from the Fe K-edges of unlithiated $LiFe_{2-x}In_xSbO_6$ samples are shown in Figure 6 ($x = 0, 1$) with data from remaining samples shown in Figure S9 in the Supporting Information. All of the measured edges are at slightly higher energies than that of a Fe_2O_3 standard, but are consistent with the Fe^{3+}. Analogous data collected from lithiated samples (Figures 6 and S10) show a significant shift in the Fe K-edges to lower energy, consistent with reduction of the iron centers to an average oxidation state of $\sim Fe^{+2.5}$ consistent with the $Li_{2-(x/2)}Fe_{2-x}In_xSbO_6$ compositions detailed in Table S10.

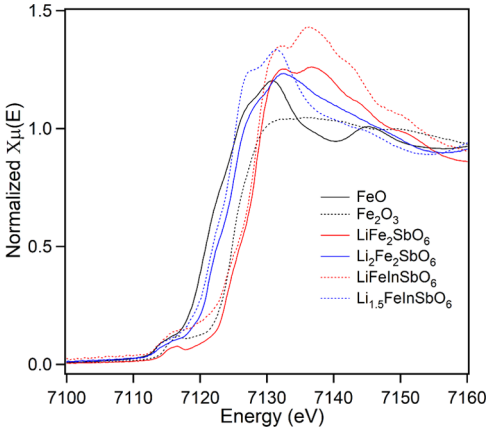

Figure 6. XANES data from the Fe K-edges of $LiFe_2SbO_6$, $Li_2Fe_2SbO_6$, $LiFeInSbO_6$, and $Li_{1.5}FeInSbO_6$ with data from FeO and Fe_2O_3 acting as standards for Fe^{2+} and Fe^{3+}, respectively.

^{57}Fe Mössbauer Data. ^{57}Fe Mössbauer data collected from $LiFe_2SbO_6$ at room temperature can be fit by two magnetic sextets of relative spectral area 94:6, as shown in Figure S11 and detailed in Table S11, in the Supporting Information. The majority feature (CS = 0.37 mm/s, B_{hf} = 37.62 T) is attributed to the magnetically ordered Fe^{3+} centers in $LiFe_2SbO_6$, described above, while the minor feature is tentatively assigned to a small quantity of α-Fe_2O_3 present in the sample but not observable by diffraction.[22]

The ^{57}Fe Mössbauer spectrum collected from $LiFeInSbO_6$ is best fit by two nonmagnetic doublets, as shown in Figure 7 and detailed in Table 1, corresponding to the octahedrally coordinated Fe^{3+} centers in $LiFeInSbO_6$. We attribute the need to use two doublets to achieve a satisfactory fit to the data, to Fe/In disorder. As shown in Figure 1a, pairs of 4*f* (Fe/In)O_6 sites share edges in the structure of $LiFeInSbO_6$. As a result, each Fe cation in a 4*f* site has either a Fe^{3+} or an In^{3+} "neighbor", with the two different possibilities yielding subtly different Mössbauer spectra.

The corresponding ^{57}Fe Mössbauer data from lithiated $Li_{1.5}FeInSbO_6$ can be fit by three doublets, as shown in Figure 7 and detailed in Table 1. Doublet 1 is consistent with Fe^{3+} while doublets 2 and 3 are consistent with Fe^{2+}, with a ratio of spectral areas of the Fe^{3+}/Fe^{2+}signals of 44:56. These data are broadly consistent with the proposed composition and refined structure of $Li_{1.5}FeInSbO_6$ described above. The presence of two distinct Fe^{2+} sites is again attributed to Fe/In disorder on the 4*f* site.

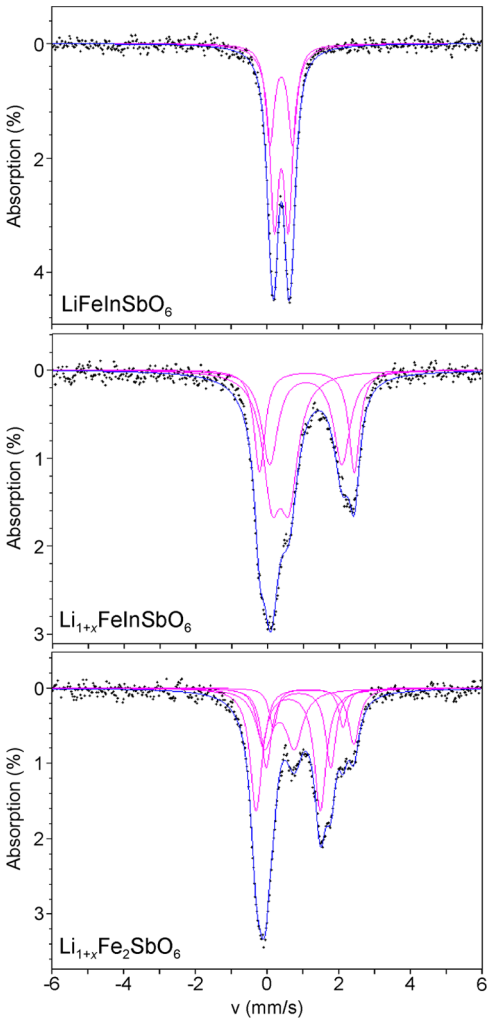

Figure 7. ^{57}Fe Mössbauer spectra collected from $LiFeInSbO_6$ (top), $Li_{1+y}FeInSbO_6$ (middle), and $Li_{1+y}Fe_2SbO_6$ (bottom) at room temperature.

The ^{57}Fe Mössbauer spectrum of $Li_2Fe_2SbO_6$ is complex and requires five doublets to fit the data adequately, as shown in Figure 7 and detailed in Table 1. Doublets 1, 2, and 3 are consistent with Fe^{2+}, doublet 4 with Fe^{3+}, and doublet 5 is intermediate between Fe^{2+} and Fe^{3+}. The cation-ordered structure of $Li_2Fe_2SbO_6$ has three distinct Fe sites, as shown in Figure 1c. The 4*f* site is 100% occupied by Fe, while the 4*f*′ and 4*e*′ sites contain 50:50 Fe/Li disordered mixtures. Considering the multiplicities and occupancies of the different Fe sites, it can be seen that $\sim 1/3$ of the Fe cations in the phase sit on each of the three sites. We attribute doublets 1 and 2 (total spectral area: 35%) to the 50:50 Fe/Li 4*e*′ site—the reduction of the Fe cations is what motivates the Fe-cation migration from the 4*f* to the 4*e* sites; thus, we would expect the 4*e*′ site to only contain reduced Fe centers. We attribute doublets 3 and 4 (total spectral area: 30%) to the 50:50 Fe/Li 4*f*′ site as the 100% Fe 4*f* site has a bond valence sum, which suggests it only contains Fe^{3+} (Table S9). Thus, we attribute doublet 5 to the 100% Fe 4*f* site. These assignments yield a ratio of 35:30:35 for the combined spectral areas of iron cations located on the 4*e*′/4*f*/4*f*′ sites consistent with the cation-ordered structure of $Li_2Fe_2SbO_6$. It has been assumed

https://doi.org/10.1021/acs.chemmater.2c03418
Chem. Mater. XXXX, XXX, XXX−XXX

Table 1. Hyperfine Parameters Extracted from the Fits to ^{57}Fe Mössbauer Spectra Collected at Room Temperature[a]

	CS (mm/s) [±0.02]	Δ (mm/s) [±0.02]	HWHM (mm/s) [±0.02]	spectral area (%) [±2]
		$LiFeInSbO_6$		
doublet 1	0.40	0.38	0.14	64
doublet 2	0.39	0.63	0.14	36
		$Li_{1.5}FeInSbO_6$		
doublet 1	0.36	0.47	0.30	44
doublet 2	1.07	2.01	0.27	33
doublet 3	1.10	2.64	0.18	23
		$Li_2Fe_2SbO_6$		
doublet 1	1.14	2.55	0.18	15
doublet 2	0.88	1.79	0.17	20
doublet 3	1.14	1.95	0.14	8
doublet 4	0.35	0.83	0.27	22
doublet 5	0.59	1.79	0.19	35

[a]CS values are stated relative to α-Fe.

that the recoil-free fraction ratio $f(Fe^{3+})/f(Fe^{2+})$ = 1.0 when considering relative spectral area ratios, hence the uncertainties associated with them.[23] The assignments are also consistent with the ∼1:1 Fe^{2+}/Fe^{3+} ratio obtained from NPD and XANES data. Thus, it can be seen that the ^{57}Fe Mössbauer data confirm the chemical and structural conclusions obtained from the diffraction and X-ray absorption data.

Chemical Oxidation. Samples of lithiated $Li_{1+y}Fe_{2-x}In_xSbO_6$ phases were stirred with I_2 in acetonitrile at room temperature for 4 h, as described above, in an attempt to reoxidize the materials (I_2/I^- = +3.5V vs Li).[24] XRD data collected from a sample of $Li_2Fe_2SbO_6$ treated in this way were unchanged, indicating no oxidative deintercalation of lithium occurred on exposure to iodine. In contrast, XRD data collected from $Li_{1.5}FeInSbO_6$ after treatment with iodine yielded a unit cell volume very close to that of $LiFeInSbO_6$ suggesting almost complete reoxidation of the sample. $Li_{1+y}Fe_{2-x}In_xSbO_6$ phases with intermediate x exhibited contractions in their unit cell volumes, on exposure to iodine, indicating partial reoxidation as shown in Figure S12 in the Supporting Information.

Summary of the Structural Effects of Lithiating $LiFe_{2-x}In_xSbO_6$ Phases. The data above show that In-for-Fe substitution in $LiFe_{2-x}In_xSbO_6$ phases modifies the structural response of these materials to lithiation.

NPD data show that substitution of In into $LiFe_{2-x}In_xSbO_6$ phases occurs via the formation of a simple Fe/In solid solution, with no change in structure for values up to x = 1. On insertion of lithium into $LiFe_2SbO_6$ (x = 0), to form $Li_2Fe_2SbO_6$, Fe cations migrate from 4*f* to 4*e* coordination sites and adopt a cation-ordered arrangement of Fe, Li, and mixed Fe/Li coordination sites, as shown in Figure 1c. In contrast, lithiation of $LiFeInSbO_6$ (x = 1) occurs via the simple insertion of lithium, to further fill the partially occupied tetrahedral 4*g* sites, with no accompanying migration of Fe cations. Partially substituted $LiFe_{2-x}In_xSbO_6$ (x = 0.25, 0.5, 0.75) phases exhibit levels of Fe migration on lithiation, which decline with increasing In content (increasing x), but only the x = 0 phase exhibits a long-range cation-ordered structure.

Comparison of the crystal structures of $LiFe_2SbO_6$ and $LiFeInSbO_6$ (Tables S1−S3) reveals that the presence of In^{3+} leads to a significant expansion of the 4*f* Fe/In site in $LiFeInSbO_6$ compared to the all-iron 4*f* Fe site in $LiFe_2SbO_6$. As a result, the bond valence sum[25,26] of a Fe cation on the 4*f* Fe/In site in $LiFeInSbO_6$ is Fe+2.34 compared to Fe+2.82 for the 4*f* Fe site in $LiFe_2SbO_6$. The expansion of the 4*f* Fe/In site means that it has a size that is intermediate between that suitable to accommodate Fe^{3+} (smaller) and Fe^{2+} (larger). As a consequence, the $LiFeInSbO_6$ framework does not need to distort by much when some of the Fe^{3+} cations are reduced to Fe^{2+} on Li insertion, as demonstrated by the modest expansion of this site on the formation of $Li_{1.5}FeInSbO_6$ (BVS = 1.97, Table S9).

Following the same logic, it can be seen that the small size of the 4*f* Fe site in $LiFe_2SbO_6$ means this material must undergo a much larger distortion of its Li−Fe−Sb−O framework to accommodate the Fe^{2+} cations formed on Li insertion. The lattice expansion required to accommodate the Fe^{2+} cations on the original 4*f* cation sites, in a manner analogous to that observed for $Li_{1.5}FeInSbO_6$, appears too energetically expensive, so instead some of the reduced Fe cations migrate to larger coordination sites within the framework, resulting in the observed cation-ordered structure of $Li_2Fe_2SbO_6$. Thus, we can see that it is the expansion of the framework (particularly the 4*f* Fe/In coordination sites) on the substitution of In^{3+} for Fe^{3+} that suppresses Fe migration on reduction.

Electrochemical Data. CV data were collected from pristine samples of $LiFe_2SbO_6$, $LiFe_{1.5}In_{0.5}SbO_6$, and $LiFeInSbO_6$ in the ranges 1.25−3.75 V (Figures 8), 1−3.5 and 1.5−3.5 V (Figures S13 and S14 in the Supporting Information) to establish the redox behavior of the materials. It was observed that scanning to potentials of less than 1.25 V led to large anomalous reductive events, attributed to reaction with the electrolyte. In contrast, cycles over the potential range 1.5−3.5 V show much smaller levels of redox activity than those over the range 1.25−3.75 V, suggesting the former range did not probe sufficiently reducing potentials to reduce the Fe centers. Thus, electrochemical cycling measurements were collected over the range 1.25−3.75 V (Figure 9) to characterize the electrochemical behavior of the $LiFe_{2-x}In_xSbO_6$ phases. It should be noted that none of the electrochemical data collected from any of the $LiFe_{2-x}In_xSbO_6$ samples showed any evidence for oxidative lithium extraction, with no oxidation features observed at potentials greater than 3.5 V.

Electrochemical Analysis of $LiFe_2SbO_6$. On sweeping the potential down from 3.75 V, the CV data collected from pristine $LiFe_2SbO_6$ (Figure 8) exhibit a large reduction event, starting at ∼ 2.2 V and maximum at 1.7 V, which does not have

https://doi.org/10.1021/acs.chemmater.2c03418
Chem. Mater. XXXX, XXX, XXX−XXX

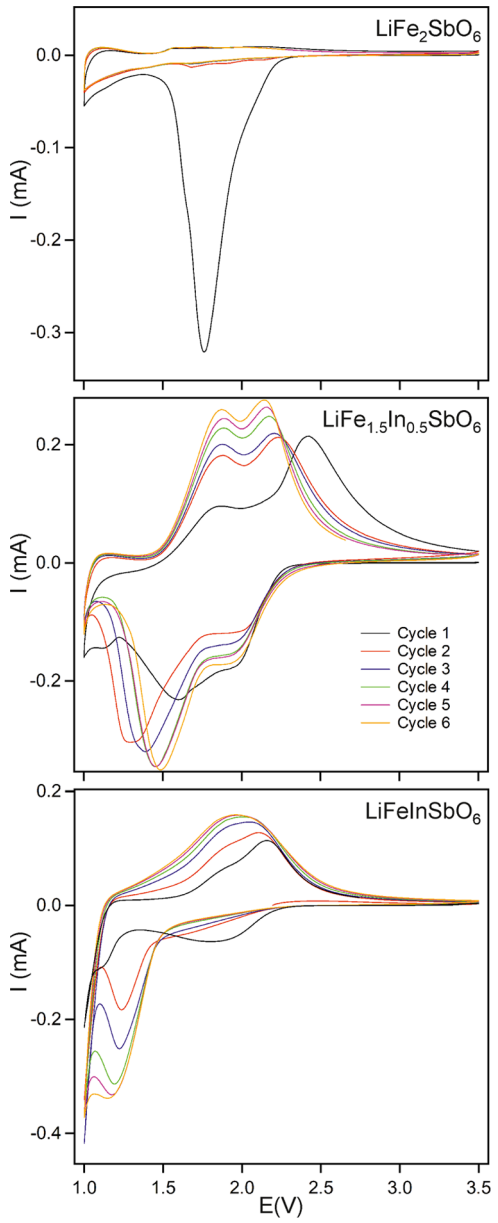

Figure 8. Cyclic voltammograms collected from $LiFe_{2-x}In_xSbO_6$ (x = 0, 0.5, 1) between 1.25 and 3.75 V. Different colors indicate sequential voltage cycles.

a corresponding oxidative feature on the return cycle. This irreversible reduction behavior is also seen in the cyclic voltammetry data collected in the other potential ranges (Figures S13 and S14). We interpret this irreversible reductive event as the migration of Fe cations and the formation of the cation-ordered phase of $Li_2Fe_2SbO_6$ observed after the treatment of $LiFe_2SbO_6$ with *n*-BuLi.

The resistance of $Li_2Fe_2SbO_6$ to subsequent reoxidation suggests that the ordering of the Fe^{3+} and Fe^{2+} cations in the framework (indicated by the bond valence sums of the cations sites in Table S9) acts to prevent further changes to the oxidation states of the Fe cations, making the ordered system electrochemically inert.

Electrochemical Analysis of $LiFeInSbO_6$. CV data collected from pristine $LiFeInSbO_6$ exhibit a slightly anomalous first cycle (Figure 8) with subsequent cycles showing a single reduction feature below 2.5 V and a corresponding broad oxidation above 1.7 V, consistent with the redox cycling of the Fe cations without cation migration.

On repeated cycling, the capacity of $LiFeInSbO_6$ drops from 42 mAh g^{-1} (0.62 Li per fu) on cycle 2 to 30 mAh g^{-1} (0.44 Li per fu) after 30 cycles, recovering to 35 mAh g^{-1} (0.52 Li per fu) after 50 cycles, as shown in Figure 9, values broadly consistent with the $Li_{1.5}FeInSbO_6$ formula of the chemically lithiated phase described above.

Electrochemical Analysis of $LiFe_{1.5}In_{0.5}SbO_6$. The electrochemical behavior of $LiFe_{1.5}In_{0.5}SbO_6$ is complex. CV data collected from a pristine sample of $LiFe_{1.5}In_{0.5}SbO_6$ (Figure 8) show an anomalous first cycle. We attribute this feature to the migration of Fe cations from 4*f* to 4*e* sites, as ~25% of the Fe cations in chemically lithiated $Li_{1.75}Fe_{1.5}In_{0.5}SbO_6$ are observed to be on 4*e* sites, arranged in a disordered manner. CV data from subsequent redox cycling of $LiFe_{1.5}In_{0.5}SbO_6$ exhibit two distinct reduction events (2.3−1.8 and 1.8−1.25 V) and two corresponding oxidations (1.25−2.05 and 2.05−3 V). These features can also be clearly seen in the CV data collected between 1 and 3.5 V (Figure S13).

Cycling capacity data (Figure 9) show the initial capacity of $LiFe_{1.5}In_{0.5}SbO_6$ is 54 mAh g^{-1} (0.73 Li per fu), consistent with the $Li_{1.75}Fe_{1.5}In_{0.5}SbO_6$ formula of the chemically lithiated material. However, on repeated redox cycling, the capacity drops sharply, to give a capacity of 37 mAh g^{-1} (0.5 Li per fu) after 20 cycles, with this latter value maintained for the following 80 cycles (Figure 9). Close inspection of the CV and capacity data reveals the decline in the overall capacity of the material arises from a decline in the capacity of the higher potential redox couple (reduction 2.3−1.8 V; oxidation 2.05−3 V), rather than a general degradation of electrochemical performance. This is most clearly seen in the decline in the magnitude of the oxidation peak centered at 2.35 V in the CV data and a change in the shape of the charging curve in the cycling data showing a decline in the high voltage capacity of the material. This latter feature is highlighted by separating the total charging capacity of $LiFe_{1.5}In_{0.5}SbO_6$ into two voltage windows, 1.25−2.05 and 2.05−3.75 V, which are plotted along with the total capacity in Figure 9.

To explain these observations, we propose a model in which 25% substitution of Fe by In partially suppresses the migration of Fe cations on reduction so that after the first reduction cycle $Li_{1+x}Fe_{1.5}In_{0.5}SbO_6$ is structurally inhomogeneous on a short length scale, containing regions in which reduction-induced 4*f*-4*e* cation migration has occurred extensively, and regions in which the parent structure has been maintained.

We further propose that a 25% substitution of In cations is sufficient to stop the migrated cations from adopting the cation-ordered structure observed for $Li_2Fe_2SbO_6$, so the Fe cations in the "migration regions" remain redox-active, albeit with a different redox potential to the Fe cations in the original parent structure. We therefore attribute the high-potential redox couple (reduction 2.3−1.8 V; oxidation 2.05−3 V) to Fe cations in the migration regions, and the low-potential redox couple (reduction 1.8−1.25 V; oxidation 1.25−2.05 V) to Fe cations in regions with low levels of cation migration. The decline in the capacity of the high-potential redox couple on repeated electrochemical cycling suggests that the repeated reduction and oxidation of the Fe centers facilitate a structural reorganization in some of the migration regions to form the cation-ordered redox-inactive arrangement adopted by

https://doi.org/10.1021/acs.chemmater.2c03418
Chem. Mater. XXXX, XXX, XXX−XXX

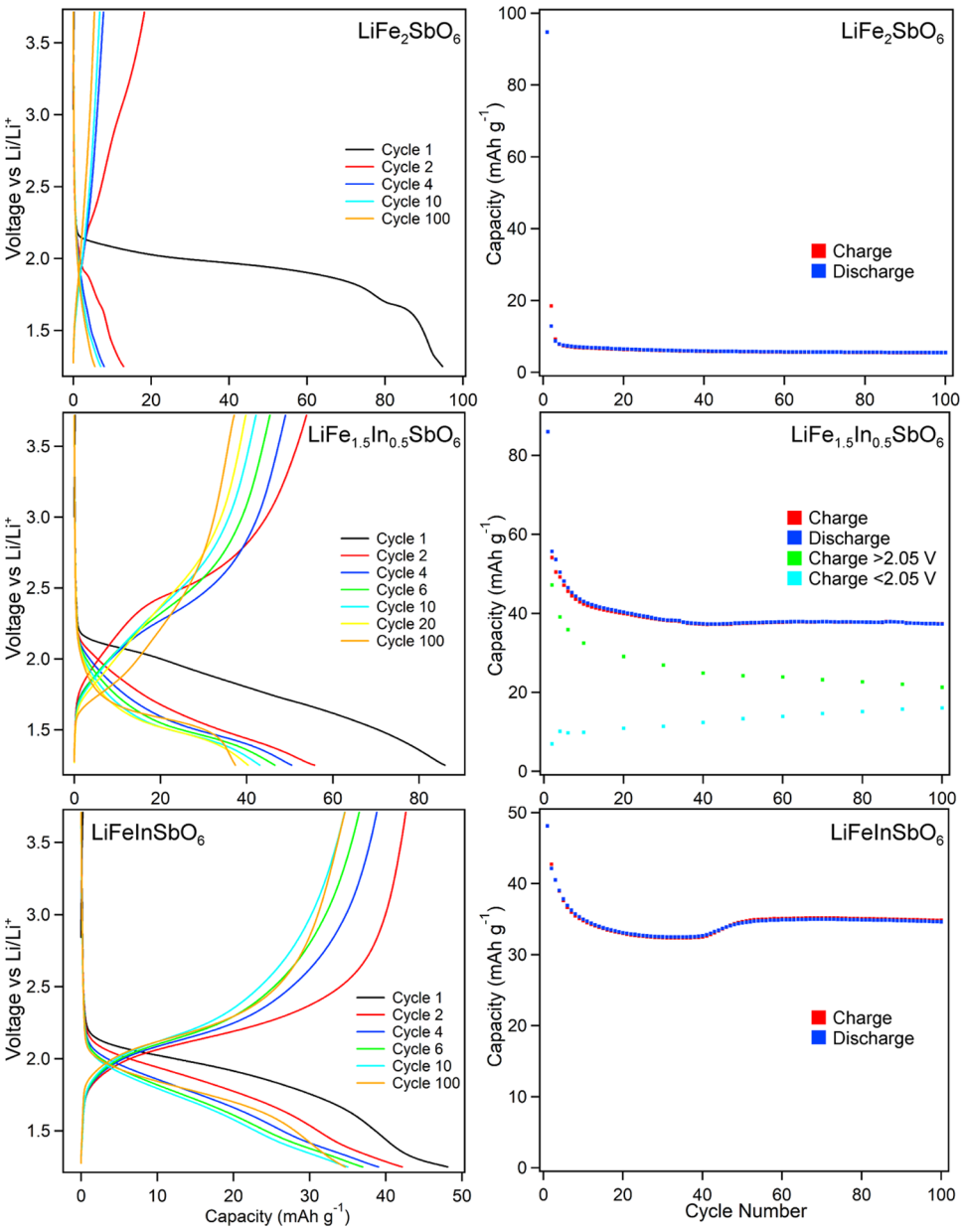

Figure 9. Capacity data collected from $LiFe_{2-x}In_xSbO_6$ (x = 0, 0.5, 1) phases while cycling between 1.25 and 3.75 V.

$Li_2Fe_2SbO_6$, thus accounting for the loss of high-potential capacity on repeated cycling.

CONCLUSIONS

Reduction of the Fe^{3+} phase, $LiFe_2SbO_6$, via Li insertion drives the site migration of some of the reduced Fe^{2+} cations to larger coordination sites within the $Li_{1+x}Fe_2SbO_6$ framework and leads to the formation of a long-range, cation-ordered, and charge-ordered structure, which prevents reoxidation of the material, and thus redox cycling.

Substitution of 50% of the Fe cations by In^{3+} leads to an expansion of the Fe coordination sites, making them more suitable for Fe^{2+} and thus suppresses the cation migration process on reduction, allowing repeated Li insertion/removal cycles. Intermediate levels of In substitution (25%) partially suppress cation migration and prevent the initial formation of a long-range cation-ordered structure, allowing a relatively high initial cycling capacity. However, repeated redox cycling leads to an ordering of migrated cations and a significant drop in electrochemical capacity. Thus, the introduction of In^{3+} can facilitate the redox cycling of this Fe-based cathode material by preventing Fe-cation migration, although the replacement of Fe by a redox-inactive In lowers the maximum theoretical capacity of the material.

ASSOCIATED CONTENT

Supporting Information

The Supporting Information is available free of charge at https://pubs.acs.org/doi/10.1021/acs.chemmater.2c03418.

Structural and XANES data, characterization of $LiFe_{2-x}In_xSbO_6$ and $Li_{1+y}Fe_{2-x}In_xSbO_6$ (x = 0, 0.25, 0.5, 0.75) phases, Mössbauer data from $LiFe_2SbO_6$, and chemical reoxidation cyclic voltammetry data from $LiFe_{2-x}In_xSbO_6$ (x = 0, 0.5, 1) (PDF)

https://doi.org/10.1021/acs.chemmater.2c03418
Chem. Mater. XXXX, XXX, XXX−XXX

AUTHOR INFORMATION

Corresponding Author

Michael A. Hayward − *Department of Chemistry, University of Oxford, Inorganic Chemistry Laboratory, Oxford OX1 3QR, U.K.; The Faraday Institution, Didcot OX11 0RA, U.K.;* orcid.org/0000-0002-6248-2063; Email: michael.hayward@chem.ox.ac.uk

Authors

Xabier Martínez de Irujo Labalde − *Department of Chemistry, University of Oxford, Inorganic Chemistry Laboratory, Oxford OX1 3QR, U.K.; The Faraday Institution, Didcot OX11 0RA, U.K.*

Heather Grievson − *The Faraday Institution, Didcot OX11 0RA, U.K.; Department of Materials Science and Engineering, University of Sheffield, Sheffield S1 3JD, U.K.*

Josie-May Mortimer − *The Faraday Institution, Didcot OX11 0RA, U.K.; Department of Materials Science and Engineering, University of Sheffield, Sheffield S1 3JD, U.K.*

Samuel G. Booth − *The Faraday Institution, Didcot OX11 0RA, U.K.; Department of Materials Science and Engineering, University of Sheffield, Sheffield S1 3JD, U.K.;* orcid.org/0000-0001-7643-4196

Alex Scrimshire − *Materials and Engineering Research Institute, Sheffield Hallam University, Sheffield S1 1WB, U.K.*

Paul A. Bingham − *Materials and Engineering Research Institute, Sheffield Hallam University, Sheffield S1 1WB, U.K.*

Emmanuelle Suard − *Institut Laue-Langevin - 71 avenue des Martyrs, 38000 Grenoble, France;* orcid.org/0000-0001-5966-5929

Serena A. Cussen − *The Faraday Institution, Didcot OX11 0RA, U.K.; Department of Materials Science and Engineering, University of Sheffield, Sheffield S1 3JD, U.K.*

Complete contact information is available at: https://pubs.acs.org/10.1021/acs.chemmater.2c03418

Author Contributions

The manuscript was written through contributions of all authors.

Notes

The authors declare no competing financial interest.

ACKNOWLEDGMENTS

This work was supported by the Faraday Institution project FutureCat (grant no. FIRG017). Experiments at the Diamond Light Source were performed as part of the Block Allocation Group award "Oxford Solid State Chemistry BAG to probe composition−structure−property relationships in solids" (CY25166).

REFERENCES

(1) Whittingham, M. S. Ultimate Limits to Intercalation Reactions for Lithium Batteries. *Chem. Rev.* **2014**, *114*, 11414−11443.

(2) Whittingham, M. S. Lithium batteries and cathode materials. *Chem. Rev.* **2004**, *104*, 4271−4301.

(3) Liu, J.; Bao, Z. N.; Cui, Y.; Dufek, E. J.; Goodenough, J. B.; Khalifah, P.; Li, Q. Y.; Liaw, B. Y.; Liu, P.; Manthiram, A.; Meng, Y. S.; Subramanian, V. R.; Toney, M. F.; Viswanathan, V. V.; Whittingham, M. S.; Xiao, J.; Xu, W.; Yang, J. H.; Yang, X. Q.; Zhang, J. G. Pathways for practical high-energy long-cycling lithium metal batteries. *Nat. Energy* **2019**, *4*, 180−186.

(4) Li, M.; Lu, J. Cobalt in lithium-ion batteries. *Science* **2020**, *367*, 979−980.

(5) Booth, S. G.; Nedoma, A. J.; Anthonisamy, N. N.; Baker, P. J.; Boston, R.; Bronstein, H.; Clarke, S. J.; Cussen, E. J.; Daramalla, V.; De Volder, M.; Dutton, S. E.; Falkowski, V.; Fleck, N. A.; Geddes, H. S.; Gollapally, N.; Goodwin, A. L.; Griffin, J. M.; Haworth, A. R.; Hayward, M. A.; Hull, S.; Inkson, B. J.; Johnston, B. J.; Lu, Z. H.; MacManus-Driscoll, J. L.; Labalde, X. M. D.; McClelland, I.; McCombie, K.; Murdock, B.; Nayak, D.; Park, S.; Perez, G. E.; Pickard, C. J.; Piper, L. F. J.; Playford, H. Y.; Price, S.; Scanlon, D. O.; Stallard, J. C.; Tapia-Ruiz, N.; West, A. R.; Wheatcroft, L.; Wilson, M.; Zhang, L.; Zhi, X.; Zhu, B. N.; Cussen, S. A. Perspectives for next generation lithium-ion battery cathode materials. *APL Mater.* **2021**, *9*, No. 109201.

(6) Zhu, X. B.; Lin, T. G.; Manning, E.; Zhang, Y. C.; Yu, M. M.; Zuo, B.; Wang, L. Z. Recent advances on Fe- and Mn-based cathode materials for lithium and sodium ion batteries. *J. Nanopart. Res.* **2018**, *20*, No. 160.

(7) McCalla, E.; Sougrati, M. T.; Rousse, G.; Berg, E. J.; Abakumov, A.; Recham, N.; Ramesha, K.; Sathiya, M.; Dominko, R.; Van Tendeloo, G.; Novak, P.; Tarascon, J. M. Understanding the Roles of Anionic Redox and Oxygen Release during Electrochemical Cycling of Lithium-Rich Layered Li_4FeSbO_6. *J. Am. Chem. Soc.* **2015**, *137*, 4804−4814.

(8) Bordet-Le Guenne, L.; Deniard, P.; Lecerf, A.; Biensan, P.; Siret, C.; Fournes, L.; Brec, R. Intrinsic instability of Fe^{4+} in electrochemically oxidized ramsdellite and orthorhombic $Li_{1-x}H_xFeO_2$. *J. Mater. Chem.* **1999**, *9*, 1127−1134.

(9) Masese, T.; Tassel, C.; Orikasa, Y.; Koyama, Y.; Arai, H.; Hayashi, N.; Kim, J.; Mori, T.; Yamamoto, K.; Kobayashi, Y.; Kageyama, H.; Ogumi, Z.; Uchimoto, Y. Crystal Structural Changes and Charge Compensation Mechanism during Two Lithium Extraction/Insertion between Li_2FeSiO_4 and $FeSiO_4$. *J. Phys. Chem. C* **2015**, *119*, 10206−10211.

(10) Shannon, R. D. Revised effective ionic radii and systematic studies of interatomic distances in halides and chalcogenides. *Acta Cryst.* **1976**, *A32*, 751−766.

(11) Armstrong, A. R.; Tee, D. W.; La Mantia, F.; Novak, P.; Bruce, P. G. Synthesis of tetrahedral $LiFeO_2$ and its behavior as a cathode in rechargeable lithium batteries. *J. Am. Chem. Soc.* **2008**, *130*, 3554−3559.

(12) Hirayama, M.; Tomita, H.; Kubota, K.; Kanno, R. Structure and electrode reactions of layered rocksalt $LiFeO_2$ nanoparticles for lithium battery cathode. *J. Power Sources* **2011**, *196*, 6809−6814.

(13) Padhi, A. K.; Nanjundaswamy, K. S.; Goodenough, J. B. Phospho-olivines as positive-electrode materials for rechargeable lithium batteries. *J. Electrochem. Soc.* **1997**, *144*, 1188−1194.

(14) Martínez de Irujo-Labalde, X.; Scrimshire, A.; Bingham, P. A.; Suard, E.; Hayward, M. A. Conversion of Li_2FeSbO_5 to the Fe(III)/Fe(V) Phase $LiFeSbO_5$ via Topochemical Lithium Extraction. *Chem. Mater.* **2022**, *34*, 2468−2475.

(15) Coelho, A. A. Bruker AXS: Karlsruhe, Germany, 2016.

(16) Lagarec, K.; Rancourt, D. G. *Recoil: Mössbauer Spectral Analysis Software for Windows*, 1998.

(17) Ravel, B.; Newville, M. ATHENA and ARTEMIS: Interactive graphical data analysis using IFEFFIT. *Phys. Scr.* **2005**, *T115*, 1007−1010.

(18) Flynn, S.; Sanghvi, S.; Nisbet, M. L.; Griffith, K. J.; Zhang, W. G.; Halasyamani, P. S.; Haile, S. M.; Poeppelmeier, K. R. $LiIn_2SbO_6$: A New Rutile-Related Structure Type with Unique Ion Channels. *Chem. Mater.* **2020**, *32*, 4785−4794.

(19) Flynn, S.; Wang, Y. R.; Griffith, K. J.; Poeppelmeier, K. R. The crystal structure of $LiSc_2SbO_6$. *J. Solid State Chem.* **2021**, *304*, No. 122615.

(20) Campbell, B. J.; Stokes, H. T.; Tanner, D. E.; Hatch, D. M. ISODISPLACE: a web-based tool for exploring structural distortions. *J. Appl. Crystallogr.* **2006**, *39*, 607−614.

(21) Stokes, H. T.; Hatch, D. M.; Campbell, B. J. *ISOTROPY Software Suite*, 2007.

(22) van der Woude, F. Mössbauer effect in α-Fe_2O_3. *Phys. Status Solidi* **1966**, *17*, 417−432.

(23) Zhang, H. L. Advances of ferrous and ferric Mossbauer recoilless fractions in minerals and glasses. *Geosci. Front.* **2022**, *13*, No. 101316.
(24) Wizansky, A. R.; Rauch, P. E.; Disalvo, F. J. Powerful oxidizing-agents for the oxidative deintercalation of lithium from transition-metal oxides. *J. Solid State Chem.* **1989**, *81*, 203−207.
(25) Brese, N. E.; O'Keeffee, M. Bond-Valence Parameters for Solids. *Acta Crystallogr., Sect. B: Strucut. Sci.* **1991**, *47*, 192−197.
(26) Brown, I. D.; Altermatt, D. Bond-Valence Parameters Obtained from a Systematic Analysis of the Inorganic Crystal Structure Database. *Acta Crystallogr., Sect. B: Strucut. Sci.* **1985**, *41*, 244−247.

https://doi.org/10.1021/acs.chemmater.2c03418
Chem. Mater. XXXX, XXX, XXX−XXX